Accepted Manuscript

Check for updates

PCCP

ARTICLE TYPE

Vibrational relaxation rate coefficients in CS-He collisions up to the dissociation limit: mixed quantum-classical calculations and neural network predictions

Marco Pezzella,[a] Fernando Pirani,[b] Massimiliano Bartolomei,[c] Qizhen Hong,[d] François Lique,[e] Loriano Storchi*[a] and Cecilia Coletti*[a]

Rate coefficients for the process $CS(v) + He \rightarrow CS(v - \Delta v) + He$ with $\Delta v = 1, 2, 3$ and for v up to 45 were calculated in the 80 K - 5000 K temperature using a mixed quantum-classical (MQC) method. The dataset was then completed using a Neural Network (NN) model, trained on the MQC rate coefficients. The reliability of the MQC method was first verified by comparing the new MQC results with initially state-selected ro-vibrational rate coefficients up to $v = 2$ computed with the vibrational close-coupling infinite-order sudden (VCC-IOS) method [Lique & Spielfiedel *Astronomy & Astrophysics*, 2007, **462**, 1179] employing the same potential energy surface (PES). To enable calculations for higher vibrationally excited states, a new analytical PES was developed that is suitable even under large bond distortions.

1 Introduction

The study of inelastic molecular collisions is essential for modelling non-equilibrium physical environments, from plasmas and (exo)planetary atmosphere composition and dynamics to the characterisation of the interstellar medium (ISM).[1–8] Non-local thermal equilibrium (non-LTE) conditions require models that rely on extensive sets of state-to-state collisional data, which are usually impossible to obtain from experiments alone.[9]

Therefore, the theoretical approach is the necessary way to proceed: collisional information is obtained from molecular dynamics simulations using accurate potential energy surfaces (PESs), which describe the interactions between colliding particles. When available, these theoretical results can be compared with experimental data to assess the reliability of the adopted computational methods. A variety of techniques can be used to describe nuclear motion and compute state-to-state collisional cross sections and rate coefficients. Full quantum methods represent the gold standard as they incorporate all possible quantum effects. However, these methods are computationally expensive and their cost increases dramatically with the number of molecular quantum states considered in the calculation, restricting their application to systems where few quantum states are accessible or when the excitation of small and medium sized rigid molecules is induced by light colliders such as He or H_2, unless approximations are introduced. Methods based on classical mechanics, mostly Quasi-Classical trajectory approaches (QCT), are often the alternative. They can be readily scaled for large systems and are easily parallelisable. Nevertheless, these methods inherently neglect quantum effects and schemes for the assignment of the final quantum states need to be applied, whose accuracy, particularly for vibrational states, is still debated.[10,11]

The mixed quantum-classical (MQC) approach[12,13] represents an effective compromise between fully quantum and classical methodologies. In this framework, the degrees of freedom exhibiting the most significant quantum behaviour are treated quantum mechanically, while the remaining ones are treated classically. This enables the inclusion of the quantum effects of interest with a consistent reduction in computational cost. In recent years, the original MQC formalism has been further developed and refined, in applications where rotations (e.g.[14] and references therein) or vibrations (e.g.[15] and references therein) constitute the quantum subset.

In the modelling of ISM or exoplanet atmospheres, there is a growing need to extend the the database of available rotationally resolved rate coefficients data for collision-induced transitions between ro-vibrational levels across a large number of species. Indeed, results from full quantum simulations have been obtained

a Dipartimento di Farmacia, Universitá G. d'Annunzio Chieti-Pescara, Via dei Vestini, 66100 Chieti, Italy. E-mail: cecilia.coletti@unich.it; loriano.storchi@unich.it

b Dipartimento di Chimica, Biologia e Biotecnologie, Universitá di Perugia, via Elce di Sotto 8, 06123 Perugia, Italy.

c Instituto de Física Fundamental - CSIC, C/ Serrano 123, Madrid, Spain.

d State Key Laboratory of High Temperature Gas Dynamics, Institute of Mechanics, Chinese Academy of Sciences, 100190 Beijing, China.

e Univ Rennes, CNRS, IPR (Institut de Physique de Rennes) – UMR 6251, 35000 Rennes, France.

49 for a variety of systems, [16–21] but are often limited to cold temperature conditions, mainly addressing the quenching of rotational states in the ground vibrational state. However, recent years have seen the detection of a growing number of vibrationally excited molecules, making the availability of comprehensive vibrational quenching and excitation rate coefficients an urgent requirement. Indeed, in the past decade, we have undergone a revolution in our ability to observationally study the molecular Universe. The high resolution of new telescopes such as Atacama Large Millimeter/submillimeter Array (ALMA) and James Webb Space Telescope (JWST) enables very detailed observations of small astrophysical bodies such as planetary atmospheres, cometary comae, and exoplanets as well as interstellar environments such as molecular clouds and protoplanetary disks. In particular, infrared observations of vibrational molecular signatures, boosted by the MIRI and NIRSPEC instruments on JWST, are flourishing.

Using MQC methods, where the vibrational motions are treated quantum mechanically while rotations and translations are described classically, can be highly effective in such cases. Indeed, this approach has been used to successfully reproduce and extend experimental results on the vibrational quenching of Earth's atmospheric species (N_2, CO, and O_2) through collisions with atoms and diatomic molecules. [22–26]

Among diatomic molecules frequently detected in astrophysical environments, carbon monosulfide (CS) is of particular interest, as it has been detected in interstellar molecular clouds, circumstellar envelopes and protoplanetary disks. [27–33] More recently, CS has also been identified in exoplanetary atmospheres as an intermediate species in the photochemical formation of SO_2. [34] Molecular collisions involving CS have been studied by Lique and coworkers (CS-He collisions), [35,36], and by different groups (CS-H_2 collisions). [37–40] The results from Lique and coworkers for CS-He collisions are especially relevant, as they provide detailed insights into ro-vibrational excitation processes: first they developed an intermolecular PES to study rotational quenching of CS, [35] and then extended their work to include the first two excited vibrational states (this work will be referred as 07LiSp hereafter). [36] Rate coefficients for inelastic collisions were calculated using the vibrational close-coupling infinite-order sudden approximation (VCC-IOS) quantum method [41,42] and made available through the BASECOL database. [43]

In this work we focus on CS-He inelastic collisions. We take on the PES developed in Ref. [36], briefly described in Section 3, and apply the MQC method, described in Section 2, to calculate the rate coefficients for the same vibrational transitions for which VCC-IOS results are available. This enables us to directly compare the performance of the MQC and VCC-IOS scattering approaches (Section 5.1). We then develop a new intermolecular analytical PES, based on the Improved Lennard-Jones model [44] (Section 3.2), which can describe larger deformations of the CS molecule. This new PES can therefore be used to obtain vibration-to-translation/rotation (V-T/R) rate coefficients for highly vibrationally excited states of CS, approaching its dissociation limit. Using the ILJ PES we construct a comprehensive dataset of V–T/R rate coefficients covering all CS vibrational levels up to 45, explicitly calculated by the MQC method and completed using a Neural
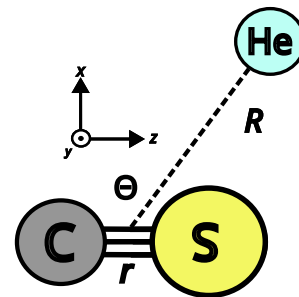

Fig. 1 Jacobi coordinates used in this work to describe the CS-He dimer interaction potential. $\Theta = 0°$ corresponds to a collinear configuration with the He atom approaching the C atom moiety and $\Theta = 180°$ sees the He atom approaching the S atom.

Network (NN) model (Section 4).

It is worth noting that, while the MQC method can yield state-to-state rate coefficients for specific ro-vibrational transitions (see Section 5.1), the primary objective of this study is to calculate a comprehensive dataset of rotationally averaged rate coefficients for the collisional quenching of vibrationally excited CS by He (see Section 5.2). This dataset includes all rate coefficients for the following processes:

$$CS(v) + He \rightarrow CS(v - \Delta v) + He, \qquad \text{with } \Delta v = 1, 2, 3$$
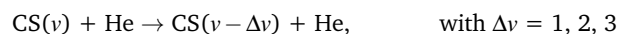
for $v = 1, \ldots, 45$ in the temperature interval 80-5000 K.

2 MQC collisional cross sections and rate coefficients

Our MQC implementation for vibrational energy transfer in atom-diatom collisions simultaneously solves the time-dependent Schrödinger equation for the vibrational degree of freedom and ro-vibrational coupling, and the classical equations of motion for the other degrees of freedom (rotation and translation). The total Hamiltonian (H) of the system in Jacobi coordinates (see Fig. 1) can be written as:

$$H = \frac{p_r^2}{2m} + v(r) + \frac{j(t)^2}{2mr^2} + \frac{1}{2\mu}\left(P_R^2 + \frac{l^2}{R^2}\right) + V(R, r, \Theta) \qquad (1)$$

where r is the diatom bond length, p_r is the molecular linear momentum, m is the molecular mass, $v(r)$ is the vibrational oscillator function, $j(t)$ is the time dependent molecular rotational angular momentum, μ is the reduced mass of the total atom-diatom system, R is the distance between the atom and the center of mass of the diatom, P_R is the system linear momentum, l is the orbital angular momentum, and $V(R, r, \Theta)$ is the interaction potential.

The quantum Hamiltonian is composed by the first three terms of Eq. 1. The rotational contribution $\frac{j(t)^2}{2mr^2}$ is present in the quantum and in the classical Hamiltonian, and, together with the effective potential V_{eff} introduced in the following, defines their interaction. $\frac{j(t)^2}{2mr^2}$ and the remaining terms compose the classical Hamiltonian. The Ehrenfest averaged potential, $V_{\text{eff}}(R, \Theta)$, is used instead of $V(r, R, \Theta)$ in the classic Hamiltonian and also couples the two Hamiltonians: [45]

$$V_{\text{eff}}(R,\Theta) = \langle \Psi | V(R,r,\Theta) | \Psi \rangle \tag{2}$$

where Ψ is the vibrational time-dependent wavefunction expressed in terms of the rotationally distorted vibrational basis ϕ_v:

$$\Psi(r,t) = \sum_v a_v(t) \phi_v(r,t) e^{\frac{-iE_v t}{\hbar}} \tag{3}$$

with a_v representing the expansion coefficients for a generic vibrational level v, E_v its energy, and $\hbar$ the reduced Planck constant. $\phi_v(r,t)$ is expressed as:

$$\phi_v(r,t) = \phi_v^0(r) + \sum_{v' \neq v} \phi_{v'}^0(r) \frac{H_{v'v}}{E_v - E_{v'}} \tag{4}$$

where $\phi_v^0(r)$ denotes eigenfunctions of the radial one-dimensional Schrödinger equation based on the rotationless intramolecular potential, and $H_{v'v}$ is the first order centrifugal stretching term:

$$H_{v'v} = -j(t)^2 m^{-1} r_{\text{eq}}^{-3} < \phi_{v'}^0 | r - r_{\text{eq}} | \phi_v^0 > \tag{5}$$

with r_{eq} being the diatom equilibrium distance.

The coefficients a_v are obtained by plugging Eq. 3 and Eq. 4 into the time-dependent Schrödinger equation, and propagating in time the following set of coupled equations together with the classical equations:

$$i\hbar \frac{da_v(t)}{dt} = E_v a_v + \sum_{v'} a_{v'}(t) \left[\langle \phi_v | V(r,R,\Theta) | \phi_{v'} \rangle - 2i\hbar \frac{d\ln j(t)}{dt} \frac{H_{v'v}}{E_{v'} - E_v} \right] \tag{6}$$

The determination of both $H_{v'v}$ and $\langle \phi_{v'} | V(R,r,\Theta) | \phi_v \rangle$ (for which $V(R,r,\Theta)$ is expanded in a Taylor series around r_{eq}) requires the calculation of the matrix coupling elements between vibrational states $M_{v'v}$:

$$M_{v'v} = \sum_k \langle \phi_{v'}^0 | \frac{\Delta r^k}{r_{\text{eq}}} | \phi_v^0 \rangle \tag{7}$$

where $\Delta r = r - r_{\text{eq}}$. Here we considered terms up to $k = 3$.

The probability for the vibrational transition $v_i \rightarrow v_f$ can be obtained as $P_{v_i \rightarrow v_f} = |a_{v_f}(\infty)|^2$ and depends on the initial conditions (i.e. the initial random values of angle and action) of the particular trajectory considered.

The total energy conservation and micro-reversibility principle imposing that $P_{v_i \rightarrow v_f}(E) = P_{v_f \rightarrow v_i}(E)$ are guaranteed by the utilisation of a symmetrisation procedure [13] which assigns a total energy E to a specific transition, so that:

$$E = E_{v_i} + E_{\text{cl}} + \frac{1}{2}\Delta E + \frac{\Delta E^2}{16 E_{\text{cl}}} \tag{8}$$

with $\Delta E = E_{v_f} - E_{v_i}$ and E_{cl} is the classical energy, i.e. the energy pertaining to the classical degrees of freedom, which in the present case is defined by the sum of the initial translational and rotational energies.

If we consider a specific initial ro-vibrational state (v_i, j_i) we can obtain the probability of the collisional transition to a final vibrational state v_f, by averaging over a number of trajectories N allowing a statistical sampling over the initial conditions:

$$P_{v_i, j_i \rightarrow v_f}(E) = N^{-1} \sum_i^N |a_{v_f}|^2. \tag{9}$$

The corresponding cross sections $\sigma_{v_i, j_i \rightarrow v_f}$ can then be obtained:

$$\sigma_{v_i, j_i \rightarrow v_f}(E) = \frac{\pi \hbar^2}{2\mu \left(E - E_{v_i} - E_{j_i} \right)} \sum_0^{J_{\max}} (2J+1) \tag{10}$$

$$\frac{1}{2j_i + 1} \sum_{l=|J-j_i|}^{J+j_i} P_{v_i, j_i \rightarrow v_f}(E)$$

where J is the total angular momentum, $J_{\max}$ is its maximum value, $E - E_{v_i} - E_{j_i}$ is the kinetic energy E_k. Note that the above cross sections correspond to initially state selected rotational states only, i.e. no resolution for the final rotational quantum number has been considered. However, cross sections resolved for the final rotational states can also be obtained by applying one of the binning schemes commonly used for this purpose in QCT calculations. The rate coefficients can be calculated by averaging over the Boltzmann distribution of kinetic energy as:

$$k_{v_i, j_i \rightarrow v_f}(T) = \left(\frac{8 k_B T}{\pi \mu} \right)^{\frac{1}{2}} \int_0^\infty \sigma_{v_i, j_i \rightarrow v_f}(E)(\beta E_k) e^{-\beta E_k} d(\beta E_k) \tag{11}$$

with $\beta = (k_B T)^{-1}$ where k_B is the Boltzmann constant and T the temperature.

In many applications, we are interested in rate coefficients for vibrational transitions averaged over the initial rotational quantum numbers j_i. This approach is especially suitable for heavy molecules such as CS, for which rotational spacings are small and many rotational states contribute to the relaxation process over the temperature range considered here. Under these conditions, statistical effects are expected to reduce the sensitivity of vibrational relaxation rates to the specific initial rotational state. It is therefore important to evaluate the validity of this approximation under the conditions relevant to astrochemical observations. While laboratory experiments have accessed rotational states as high as j=113 [46,47], astrochemical detections remain limited to much lower excitation. In high-excitation regions such as Orion KL, the highest detected transition of CS is $j = 26 - 25$ [48], and in colder dense cores rotational levels with $j < 10$ are typically observed. In these environments, the gas density often exceeds the critical density for rotational transitions, ensuring that the rotational population follows a Boltzmann distribution. Nevertheless, in extreme non-LTE or very low-density environments (e.g., cometary comae) state-specific rotational effects may become more important. However, as recently discussed by Bowesman et al. [49], approaches assuming rotational LTE and vibrational (or vibronic) non-LTE are expected to capture the dominant non-LTE effects observable with the James Webb Space Telescope, particularly in view of the computational infeasibility of treating the full set of rovibrational transitions explicitly. Furthermore, radiative-transfer models generally require the inclusion of higher-lying rotational levels that may be weakly populated,

even if not directly observed, as neglecting them can affect the excitation balance and lead to biased physical conditions.

To determine rotationally averaged rate coefficients, it is convenient to calculate rotationally averaged "cross sections" $\sigma_{v_i \to v_f}(E_{cl}, T_{ref})$:

$$\sigma_{v_i \to v_f}(E_{cl}, T_{ref}) = \frac{\pi \hbar^4}{4\mu (k_B T_{ref})^2 I} \int_0^{J_{max}} dJ(2J+1)$$

$$\int_0^{j_{max}} dj \int_{l=|J-j|}^{J+j} dl P_{v_i \to v_f}(J, j, l, E_{cl}) \quad (12)$$

I is the moment of inertia of the diatom. In this formulation a reference arbitrary temperature $T_{ref} = 300$ K is used, which cancels out when rate coefficients are computed:[12]

$$k_{v_i \to v_f}(T) = \left(\frac{8k_B T}{\pi \mu}\right)^{\frac{1}{2}} \int_0^\infty d(\beta \varepsilon) \exp(-\beta \varepsilon) \left(\frac{T_{ref}}{T}\right)^2 \sigma_{v_i \to v_f}(E_{cl}, T_{ref}) \quad (13)$$

with $\varepsilon = E - E_{v_i}$. The above expression is valid for de-excitation collisions.

In the following, we calculated the rate coefficients using eq. (11) to compare the coefficients obtained by the MQC method with those obtained by the VCC-IOS approach[36], and then using eq. (13) to produce the dataset of V-T/R rate coefficients for vibrational quenching in a wide temperature range. In both cases, adequate coverage of the energy spectrum is important for good sampling, which can be achieved by using denser sampling of low energies to describe low temperatures and including a representative number of points at higher energies.

We solved the combined classical and quantum coupled equations using a variable-order, variable-step Adams predictor-corrector integrator, imposing an accuracy of 1×10^{-8}.

3 Potential Energy Surfaces

3.1 CS intramolecular potential and vibrational wavefunctions

The evaluation of the matrix coupling elements in eq. 7, the vibrational wavefunction (eq. 3) and the vibrational energy levels requires the use of the rotationless vibrational wavefunctions $\phi_v^{j=0}(r, t)$ for the isolated CS molecule.

Initially, to enable comparison with the results of ref.[36], we used the same matrix elements and vibrational energy levels. These were obtained using the vibrational wavefunctions evaluated by the Fourier Grid Hamiltonian (FGH) method,[50] which is based on a CS potential energy function derived from a Rydberg-Klein-Rees (RKR) curve[51] and using the experimental spectroscopic constants from Bogey et al.[52]. The work reports matrix elements for the ground state and the first two excited vibrational states.

To determine collisional vibrational transition rate coefficients for highly excited states, we employed CS vibrational wavefunctions obtained from the recent spectroscopic model, developed by Paulose et al (hereafter referred to as JnK).[53] This model starts from Coxon & Hajigeorgiou potential energy curve,[54] with refined parameters that yield improved agreement with experimen-

tal data. Experimental vibrational energy levels were used when available through the measured active rotation–vibration energy levels procedure.[55] The model consists of 50 vibrational states up to the dissociation limit, with rotational states ranging up to $j = 257$ for $v = 0$. The energy levels for the first three vibrational states obtained by the two models agree within 0.1 cm^{-1}.

The matrix elements $M_{v_i' v_i}$ were generated using the vibrational wavefunction from Level16 program,[56] on a grid spanning $0.75 < r(\text{Å}) < 8.0$ with a step size of 0.05 Å. The resulting values differ from those reported by Lique and Spielfiedel[36] by less than 4%, which is well within the expected 10% accuracy of the method.

3.2 CS-He intermolecular potential: a new analytical PES

The quality of scattering cross sections and rate coefficients critically depends on the quality of the PES describing the interaction potential both at short and long range. In particular, long-range interactions play a fundamental role at low temperatures, where orientation effects —which originate at large intermolecular separations— can significantly influence the dynamics and outcomes of the collisions.

We again start by using the intermolecular PES developed by Lique and Spielfiedel[36], obtained through an analytical fit to ab initio points calculated at the coupled cluster level with single and double excitations and perturbative triples [CCSD(T)], using Dunning's augmented correlation-consistent quadruple-zeta basis set[57] (aug-cc-pVQZ) further augmented with diffuse [3s3p2d2f1g] bond functions. Basis set superposition error (BSSE) corrections were included following the procedure of Werner et al.[58]. The dependence on the carbon–sulfur bond length r was explicitly incorporated by evaluating the potential at three geometries, 2.4, 2.9, and 3.4 bohr. This makes the potential energy surface reliable for vibrational levels up to $v = 2$.

Throughout this work, the CS-He potential is described using a Jacobi coordinate system, where r represents the carbon–sulfur bond length, R is the distance between the He atom and the CS centre of mass, and Θ is the angle between these two vectors (Figure 1).

To address higher vibrationally excited states, we have also developed a new potential energy surface designed to be reliable for larger distortions of the CS bond.

As in previous works[15,26,59], where we determined large datasets of rate coefficients for vibrational energy transfer, we adopt an analytical model that provides a reliable representation of the interaction, both at equilibrium and for large distortions of the CS bond. This model is expressed as a combination of effective contributions, whose basic parameters have clear physical interpretations in terms of the fundamental properties of the interacting species —such as the static dipole polarizability, the number of outer-shell electrons determining its magnitude, and the permanent electric dipole moment. The numerical values of these parameters were adjusted against accurate ab initio interaction energies for the CS-He ground singlet state computed for a wide range of intermolecular distances using the CCSD(T) approach in the complete basis set (CBS) limit.

In such computations, counterpoise-corrected[60] interaction en-

326 ergies obtained using the aug-cc-pVQZ and aug-cc-pV5Z[57] basis
327 sets have been properly combined[61,62] to obtain reliable extrap-
328 olated CBS values. To also probe the dependence of the inter-
329 molecular potential on the stretching of the CS bond length be-
330 yond its equilibrium value $r_{eq}^{CS} = 2.9$ bohr, two further values (3.19
331 and 3.335 bohr) were considered. Furthermore, *ab initio* estima-
332 tions of the CS permanent dipole moment and static dipole polar-
333 izability, which are quantities needed for the analytical represen-
334 tation of the global PES (see below), have been obtained as pre-
335 viously done[63–66] for different monomers at the multireference
336 ACPF (Averaged Coupled Pair functional) level in combination
337 with the aug-cc-pV5Z basis set and as a function of the internu-
338 clear distance. In particular, the natural molecular orbitals in the
339 ACPF calculations were those from the complete active space self-
340 consistent field reference wave functions. The active space (CAS)
341 considered here is defined by distributing 18 electrons in the or-
342 bitals indicated as $(2, 3, 4)\sigma_g \ (2, 3, 4)\sigma_u \ (1, 2)\pi_u \ (1, 2)\pi_g$. The
343 $1\sigma_g \ 1\sigma_u$ core molecular orbitals were constrained to be doubly
344 occupied and excluded from the used CAS while also being fully
345 optimised. Additional estimations of the CS dipole polarizability
346 have been carried out at the CCSD(T)/aug-cc-pV5Z level of the-
347 ory. All electronic structure calculations were carried out by using
348 the Molpro 2012.1 package.[67]

349   The complete formulation of the analytical PES is provided in
350 Appendix A, and the corresponding computational subroutine is
351 available in the ESI†.

352   Figures 2 and 3 present several comparisons between the new
353 analytical PES and the *ab initio* PES derived in[36] for CS at its
354 equilibrium bond length. The contour plot shown in Fig. 2 in-
355 dicates that the two PESs exhibit a very similar overall topology,
356 with only minor differences in the shape of the potential mini-
357 mum for certain orientations. The potential cuts shown in Fig.
358 3 demonstrate excellent agreement between the current ab initio
359 estimations (calculated at the CCSD(T)/CBS level) and the two
360 PESs for the three dimer configurations considered (top three
361 panels). Both PESs accurately reproduce the predicted position
362 and depth of the potential well, with minor discrepancies, below
363 0.5 meV, occurring for V_{anal}. The two bottom panels of the same
364 figure illustrate the corresponding angular dependence of the in-
365 teraction energy at fixed intermolecular distance R values ($R = 4$
366 Å and $R = 5$ Å). In all cases, the quantitative differences in the
367 attractive region are very small (ca. 0.1 meV) and limited to a
368 few specific orientations. This also constitutes a validation of the
369 new analytical PES for small distortions of CS bond length. In-
370 deed, such good agreement between the analytical PES and the
371 ab initio points is remarkable. While this level of agreement is
372 expected for the V07LiSp PES, which was constructed by fitting
373 a large number of ab initio points at the CS equilibrium bond
374 length, the analytical PES relies solely on a limited number of
375 physically motivated parameters. The last condition is basic to
376 formulate a PES reliable in the full range of accessible molecular
377 orientations and in an extended range of molecular deformations.

378   Direct comparison with the *ab initio* data computed at the
379 CCSD(T)/CBS level is feasible only for small deviations from the
380 equilibrium bond length (see Figure S1 in the ESI†, correspond-
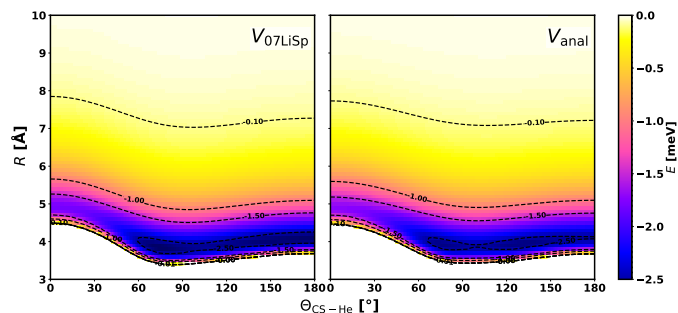381 ing to a 15% CS bond elongation). A more extensive comparison

Fig. 2 Contour plots of the new analytical potential energy surface, V_{anal} (right panel), and of the V_{07LiSp} PES[36] (left panel), both evaluated at the equilibrium bond length $r = r_{eq}^{CS}$. The minimum of V_{anal} is located at $\Theta = 78°$ and $R = 3.90$ Å, with a well depth of -2.61 meV, while for V_{07LiSp} the minimum occurs at $\Theta = 75°$, $R = 3.84$ Å, and -2.70 meV.

382 would require accounting for the increasing multireference char-
383 acter of the electronic wavefunction at larger distortions, which
384 lies beyond the scope of the present work. The figure shows
385 that the position of the potential minimum is satisfactorily repro-
386 duced, with a maximum discrepancy in the well depth of approx-
387 imately 0.5 meV.

388   Overall, the accuracy of the analytical PES, based on compari-
389 son with ab-initio points, is expected to be within 10% for small
390 deformations of the CS bond and within 30% for the largest de-
391 formations.

4   The Neural Network model

392 In recent years, machine learning (ML) techniques have been in-
393 creasingly employed to predict cross sections and rate coefficients
394 from a limited set of computed values. The requirement for ex-
395 tensive state-to-state datasets, often spanning wide temperature
396 ranges, makes data-driven prediction from a restricted number of
397 computationally expensive calculations an appealing approach.
398 Consequently, rate coefficients derived from QCT and MQC simu-
399 lations for both reactive and inelastic scattering have been mod-
400 elled using Neural Networks (NN) and Gaussian Process Regres-
401 sion (GPR) methods.[25,68–71] Both techniques have demonstrated
402 comparable predictive performance, provided they are applied
403 within the interpolation domain of the training data. However,
404 differences in training efficiency can arise depending on the size
405 of the dataset and the dimensionality of the feature space.[69]

406   In this work, we construct the dataset directly starting from
407 rate coefficients rather than on cross sections, since the rotation-
408 ally averaged cross sections (eq. 12), which depend on the refer-
409 ence temperature, do not represent intrinsic collision properties.
410 In contrast, rate coefficients can be straightforwardly related to
411 physically relevant observables, such as collisional excitation and
412 relaxation rates. Besides, we verified that building the dataset
413 starting from cross sections or from rate coefficients leads to neg-
414 ligible differences in the final results.

415   Here, an NN model was selected over a GPR one, as a com-
416 parative evaluation demonstrated its superior performance on
417 our specific datasets. To ensure a fair comparison, both mod-
418 els first underwent hyperparameter optimization via an extensive
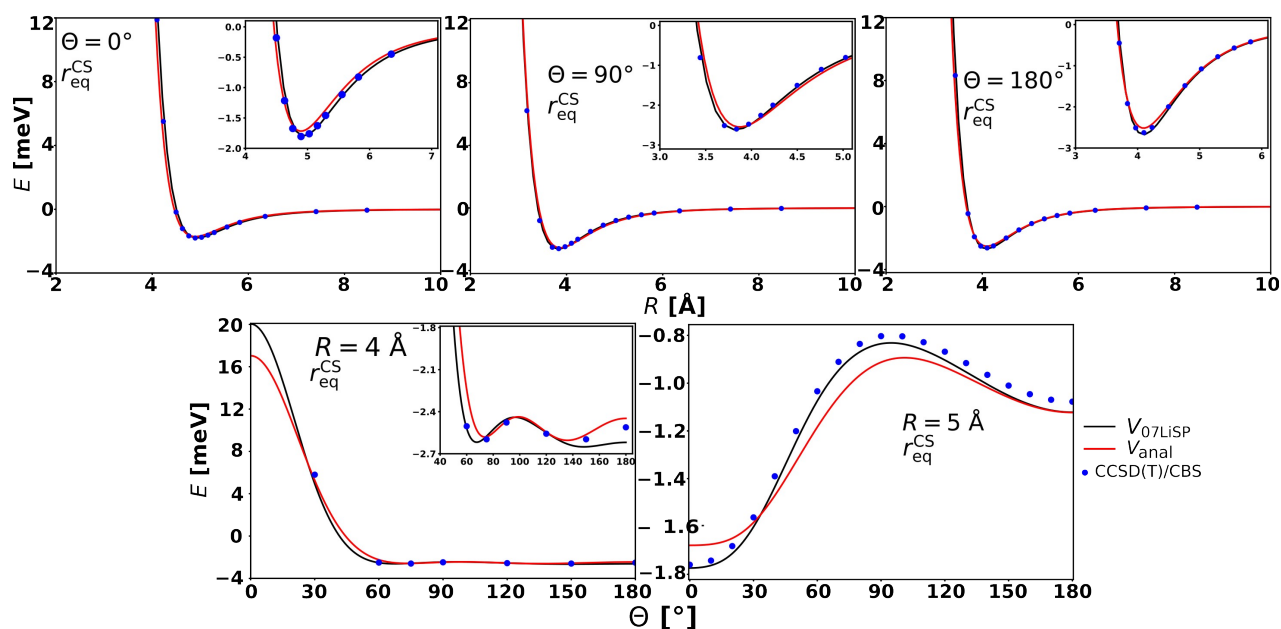419 grid search. For the GPR model, we optimized parameters includ-

Fig. 3 Potential energy cuts at the equilibrium bond length $r = r_{eq}^{CS}$ comparing the results from the V_{07LiSp} PES[36], the present analytical potential V_{anal}, and the CCSD(T)/CBS *ab initio* points.

ing the value of ν (nu) when using the Matérn kernel). For the NN model, we optimised the architecture by varying the number of dense layers and the number of neurons per layer. The performance of the optimised models was then evaluated using a Leave-One-Out Cross-Validation (LOOCV) strategy. This was applied to the three datasets of rotationally averaged rate coefficients for the CS(v) + He → CS($v - \Delta v$) + He transitions, corresponding to $\Delta v = 1, 2$, and 3. In this procedure, the model is trained on all data points in a set except one, which is kept out for testing. This process is repeated for every data point, enabling us to judge the overall effectiveness of each model. The ANN model consistently produced better predictive accuracy in these tests, resulting in its selection as the optimal model for this study.

Following this initial step, the optimal neural network architecture was identified through a two-stage grid search process designed to balance the accuracy of the predictions with the physical plausibility of the resulting output surface. In the first stage, a conventional grid search was performed on a wide range of model hyperparameters, using a standard LOOCV strategy to evaluate performance and select a smaller subset of promising candidates. The second stage involved a more refined evaluation focused on the smoothness of the final interpolated surface. To achieve this, the training data points - consisting here of all the computed rate coefficients values for each Δv - were combined with the model predictions to create a complete surface representation. The smoothness of this surface was then assessed quantitatively by calculating the mean absolute Laplacian. This metric was derived by first interpolating the scattered data points onto a regular grid and then applying a Laplacian kernel via 2D convolution to approximate the surface curvature at each point. Ultimately, models that produced a lower mean absolute Laplacian value were favoured, as this indicates a smoother and less erratic surface. This ensures that the final selection is accurate and gen-

erates physically realistic outputs. All codes can be retrieved at Ref. 72.

This two-stage optimisation process led to the selection of our final model configuration. The optimal architecture identified was a three-layer network with 256 neurons per layer ([256, 256, 256]). The model was trained using the Adam optimiser with the Mean Squared Error (MSE) loss function. Training was run for 1000 epochs for all datasets, and the model weights from the epoch that achieved the minimum training MSE were selected for the final model. The optimisation process also indicated different optimal batch sizes: a batch size of 50 was used for the $\Delta v = 1$ dataset and a batch size of 256 was employed for both the $\Delta v = 2$ and $\Delta v = 3$ datasets.

## 5 Results and discussion

5.1 Comparison between MQC and VCC-IOS rate coefficients

The availability of the results for the CS-He ro-vibrational de-excitation cross sections and rate coefficients in Ref.[36] gives us the opportunity to compare these quantities using two completely different methods: the time-independent quantum VCC-IOS of Ref.[36], and the time-dependent MQC approach of the present work.

The results by Lique and Spielfiedel[36] cover ro-vibrational transitions for $v=0$, 1, and 2, ranging from $j = 0$ to $j = 37$. The reported accuracy is within a factor of 2–3 for the ro-vibrational excitation and within a factor of 1.5 for pure rotational excitation within one vibrational manifold.

Those rate coefficients were compared with the corresponding MQC values calculated using eq. 11 obtained by running 5000 trajectories for each of the 34 initial classical energy values E_{cl}, in the interval 50 cm^{-1} - 10,000 cm^{-1}, selected on an unevenly distributed energy grid, with a higher density of points at lower

energies. These settings should ensure an accuracy of the MQC method within 20%. An initial separation of $R = 20$ Å was adopted which reflects the coordinate space extension used in Lique and Spielfiedel [36]. As mentioned in section 2, the present implementation of the MQC method does not explicitly select the final rotational state j_f of the CS molecule. However, since the VCC-IOS data include rotational states only up to $j = 37$, a histogram binning procedure was applied to enable a meaningful comparison. Specifically, the cross sections (Eq. 10) were computed by including only those trajectories leading to a final rotational energy equal to or lower than that corresponding to $j_f = 37$. Accordingly, the rate coefficients can be compared for the following process:

$$CS(v_i, j_i) + He \rightarrow CS(v_f, \sum_0^{37} j_f) + He, \qquad \text{for } v_i = 1, 2 \text{ and } v_f < v_i.$$
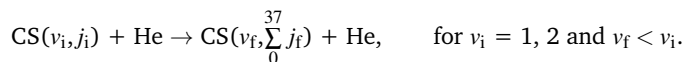
Calculations were performed for initial rotational states $j_i = 0, 1, 2, 5, 10,$ and 30 with $v_i = 1$, and for $j_i = 0, 5, 10,$ and 30 with $v_i = 2$, coupling only the first three vibrational levels. The results for these selected transitions are presented in Fig. 4, while a detailed quantitative comparison of the corresponding rate coefficients is provided in Table S1 of the ESI[†]. Figure S2 in the ESI[†] further illustrates the comparison in terms of the ratio between the MQC and VCC-IOS rate coefficients.

For processes with $\Delta v = 1$ (upper panels in Fig. 4), the agreement is excellent for the lowest initial rotational quantum numbers, regardless of the initial vibrational state and across the entire temperature range. For $j_i \leq 5$, the maximum deviation remains below 50%, which is well within the combined numerical uncertainties of both methods. The main difference between VCC-IOS and MQC data is that VCC-IOS rate coefficients are basically independent on the initial rotational excitation whereas MQC values show an increase as j_i grows, an effect which decreases with temperature. As a result, MQC and VCC-IOS rate coefficients match very well (i.e. differences are below the methods accuracy) for at least $j_i \leq 10$ in the low temperature range and nearly for all the considered j_i's for the highest temperature. This behaviour may be partly attributed to the imposed constraint of $j_f \leq 37$. Considering the rotational state distribution within the investigated temperature range, and the known propensity of vibrational relaxation processes to favour transitions with $\Delta j = j_f - j_i = 0$, with the probability decreasing rapidly as $|\Delta j|$ increases, particularly at low temperatures, this limitation is expected to have only a minor effect for the lowest j_i values. In contrast, for the highest j_i levels, where transitions populating high rotational states is more likely, an accurate description of the final rotational distribution becomes increasingly important.

It is worth noting, however, that ro-vibrational excitation rate coefficients calculated using the full close-coupling (CC) method for CO–He collisions [73] show a similar trend, with a slight increase as the initial rotational excitation of the molecule rises in the 1000–1500 K temperature range, even though those calculations are limited to $j_f \leq 14$. This behaviour suggests that a comparable dependence may also apply to the CS–He system as captured by the MQC-calculated rate coefficients.

The process involving the loss of two vibrational quanta shows a comparable behaviour; however, in this case, the best agree-
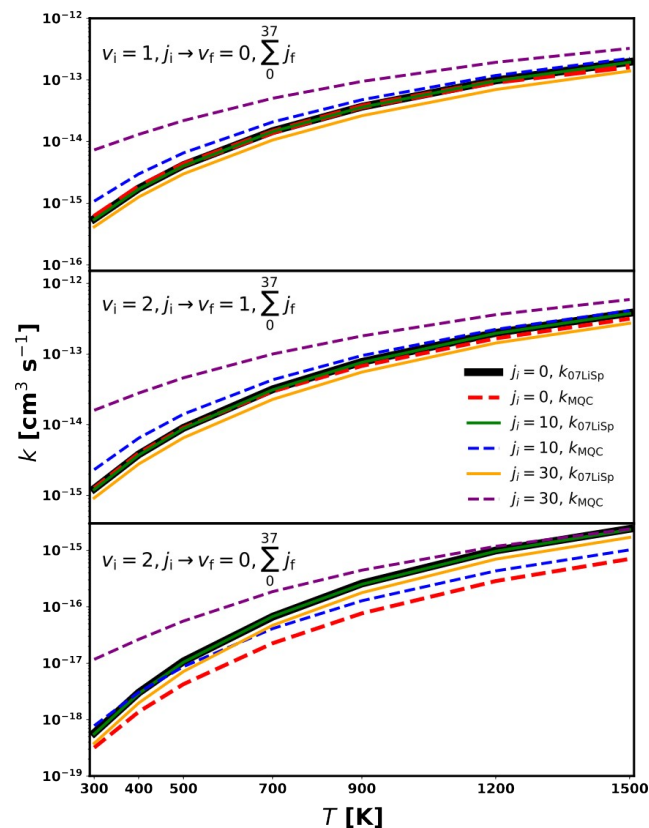

Fig. 4 MQC (dashed lines) and VCC-IOS [36] (solid lines) rate coefficients for the $CS(v_i, j_i) + He \rightarrow CS(v_f, \sum_0^{37} j_f) + He$ transition as a function of temperature.

ment is observed for $j_i > 10$ and discrepancies tend to be larger.

Although the level of agreement with the results of Lique and Spielfiedel [36] varies with the initial rotational quantum number, the fact that the present work focuses on producing a dataset of rotationally averaged vibrational de-excitation rate coefficients ensures that these differences remain within the expected accuracy of the VCC-IOS results.

5.2 Dataset of vibrational excitation rate coefficients

The rotationally averaged de-excitation rate coefficients for the process $CS(v) + He \rightarrow CS(v - \Delta v) + He$, for vibrational levels up to $v = 45$, were calculated using eq. 13 and the new analytical PES. The accuracy of the results, considering the combined uncertainties of the PES and of the MQC method, is expected to lie within 25-30% for the transitions involving lower vibrational states and within 50% for the highest ones. Figure 5 compares the MQC-calculated rate coefficients for the $CS(v = 1) + He \rightarrow CS(v = 0) + He$ transition obtained with the new V_{anal} and the 07LiSp PESs. Both surfaces yield similar temperature dependencies, while the new PES systematically predicts values larger by approximately a factor of two. This systematic increase may be related to the slightly earlier onset of the repulsive wall in the analytical PES compared to the V07LiSp PES for collisions occurring within the acceptance angular cone $\Theta < 90°$ (Fig. 3), corresponding to He approaching CS from the carbon side ($\Theta = 0°$). Given
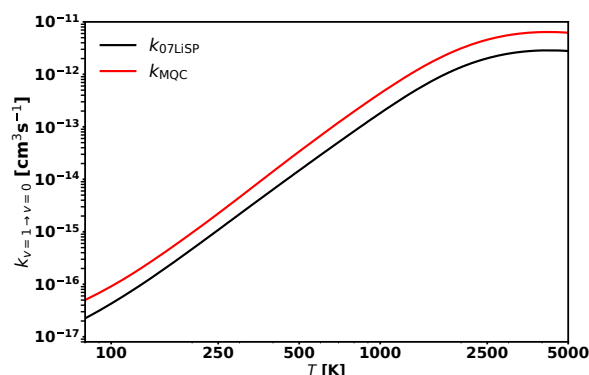
Fig. 5 MQC rate coefficients for $CS(v=1) + He \rightarrow CS(v=0) + He$ calculated using the new V_{anal} (black curve) and the 07LiSp PESs (red curve) as a function of temperature

the larger distance of the carbon atom from the molecular center of mass, such collisions are expected to be more effective in inducing vibrational energy transfer.

MQC de-excitation rate coefficients were calculated for the first three vibrational states and, starting from $v_i = 5$, every five levels up to $v_i = 45$. Above this level, the predissociative character of the vibrations caused numerical instabilities in the simulations. For each calculation, all vibrational levels within a 7000 cm^{-1} interval from v_i were coupled. The temperature range of $80 - 5,000$ K was chosen to ensure good coverage of environments ranging from the interstellar medium (ISM) to hot exoplanetary atmospheres. A total of 5000 trajectories were computed for each of the 37 values of E_{cl}, spanning the $50 - 20,000$ cm^{-1} interval on an uneven energy grid with a higher point density at low energies. All trajectories were initiated at a separation of $R = 50$ Å. Vibrational energy levels were taken from the JnK model,[53] and matrix coupling elements were obtained from the vibrational wavefunctions following the procedure described by Hong et al.[15].

Figure 6 presents the collisional relaxation rate coefficients corresponding to the loss of one (top panel), two (middle panel), and three (bottom panel) vibrational quanta over the studied temperature range. As expected, in all cases the rate coefficients increase with both the initial vibrational level—owing to the decreasing energy gap—and temperature. The latter dependence is more pronounced at low temperatures and for low vibrational states: the rate coefficients reach a plateau at progressively lower temperatures as v_i increases. Consequently, vibrational relaxation proceeds more rapidly for highly excited vibrational states at low temperatures (as expected from the stronger direct coupling between such states), while becoming nearly independent of v_i at high temperature. This temperature trend becomes increasingly pronounced as Δv grows, and the corresponding rate coefficients decrease in magnitude. The combined effect of these behaviours produces a larger variation in the rate coefficients across the temperature range for the lowest vibrational states, as illustrated in Fig. S3 in ESI†.

The dataset was completed by using the NN model as described in Section 4. Panel A of Fig. 7 shows both the MQC calculated and the predicted NN rate coefficients for the $CS(v_i) + He \rightarrow CS(v_i - 1) + He$ transitions, while panel B shows the cor-
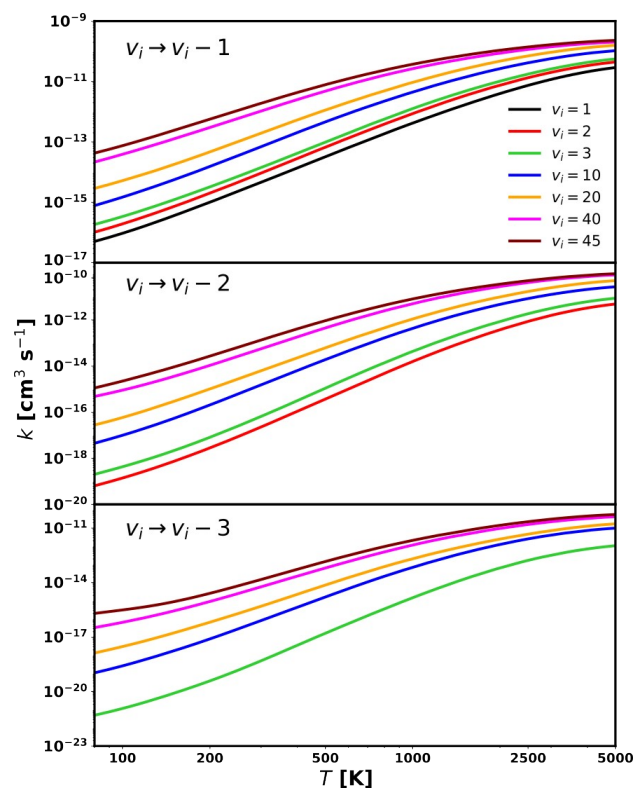

Fig. 6 MQC rate coefficients for $CS(v) + He \rightarrow CS(v - \Delta v) + He$ calculated for selected v as a function of temperature.

responding contour plot, illustrating that the NN predicted values smoothly fill in the calculated ones across the full vibrational range. Similar plots for the $v_i \rightarrow v_i - 2$ and $v_i \rightarrow v_i - 3$ transitions are provided in the ESI† (Figure S4 and S5) and exhibit the same overall behaviour. All the rate coefficients are available, together with the NN models, at Ref. 74.

6 Conclusions and further remarks

In this work, we employed a mixed quantum–classical (MQC) approach combined with a neural network (NN) scheme to construct a complete dataset for the vibrational relaxation of the CS molecule in collisions with He atoms over the 80–5000 K temperature range. Selected vibrational transitions were explicitly calculated using the MQC method, whose performance was preliminarily assessed by comparison with ro-vibrational rate coefficients obtained from the VCC-IOS approach. The agreement between the two methods is generally good, particularly for low initial rotational states. The main difference lies in their dependence on the initial rotational excitation: while VCC-IOS rate coefficients are largely independent of the initial rotational quantum number, the MQC results exhibit a moderate increase with rotational excitation.

A new analytical potential energy surface (PES) was developed using physically meaningful parameters and is expected to remain reliable even for highly excited vibrational states. The MQC-calculated rate coefficients display the expected physical behaviour, increasing with both temperature and initial vibrational level. The NN approach was then applied to extend and complete
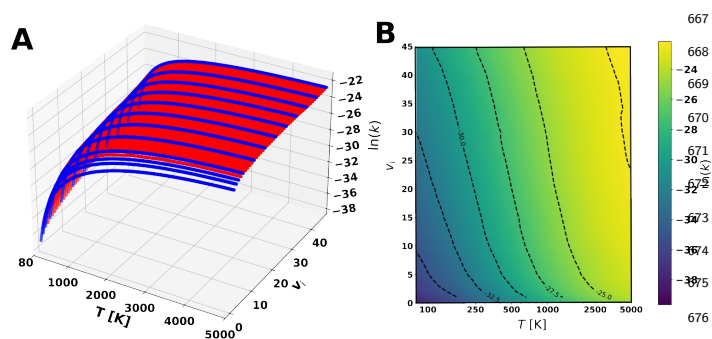
Fig. 7 MQC calculated and NN predicted rate coefficients for $CS(v_i) +$ He $\to CS(v_i - 1) +$ He. Panel A shows the calculated values (in blue) and the predicted values (in red) as functions of the initial vibrational level and temperature. Panel B presents the corresponding contour plot, displaying both the calculated and predicted rate coefficients.

the MQC dataset, yielding a smooth and physically consistent representation across the full vibrational and temperature ranges.

The resulting MQC+NN dataset provides a coherent description of CS–He collisional vibrational relaxation under a wide range of conditions relevant to astrophysical and (exo)planetary environments. This work highlights the potential of hybrid MQC (or semiclassical) and machine-learning strategies for producing accurate and comprehensive collisional datasets for complex molecular systems.

Future studies will explore the application of this approach to generate large datasets of rotationally state-resolved rate coefficients for vibrational transitions, particularly in regimes where the rotational dynamics exhibit predominantly classical behaviour.

Conflicts of interest

There are no conflicts of interest to declare.

Data availability

The data supporting this article, including the routine for the analytical PES, are available as part of the Supplementary Information or can be found in the following repositories:
Neural Network codes: CurveFittingML, 2022, https://github.com/lstorchi/CurveFittingML.
Trained Neural Network models and rate coefficient datasets: M. Pezzella, F. Pirani, M. Bartolomei, Q. Hong, F. Lique, L. Storchi and C. Coletti, DATA related to: Vibrational relaxation rate coefficients in CS-He collisions up to the dissociation limit: mixed quantum-classical calculations and neural network predictions, 2025, https://doi.org/10.5281/zenodo.17554162.

Acknowledgements

Appendix A: Formulation of the analytical PES

The analytical semi-empirical potential, V_{anal}, is made of three components:

$$V_{\text{anal}} = V_{\text{ind}} + V_{\text{ILJ}} + V_{\text{rep}}. \tag{14}$$

The first term describes the induction contribution (V_{ind}) that arises from the interaction between the permanent dipole of CS (μ_{CS}) and the induced dipole on helium that depends on its polarizability (α_{He}). This contribution is represented by the following semiempirical formula[75]:

$$V_{\text{ind}} = -\frac{\alpha_{\text{He}} \mu_{\text{CS}}^2 (1 + P_2(\Theta))}{R^6} \tag{15}$$

with $P_2(\Theta)$ being the second Legendre polynomial. The dipole is analytically described using a polynomial expression of the form:

$$\mu_{\text{CS}} = 0.7758 - 1.45\Delta r + 0.3\Delta r^2 + 0.45\Delta r^3 - 0.17\Delta r^4 \tag{16}$$

where $\Delta r = r - r_{\text{eq}}$.

V_{ILJ} represents the contribution to the interaction arising from the balance between the short-range atom-molecule size repulsion and the long-range dispersion attraction. It has been modelled according to the improved Lennard-Jones (ILJ) formulation.[44]

The V_{ILJ} contribution is expressed as the sum of pairwise interactions between He with C and S atoms. For each component, it takes the following form:

$$V_{\text{ILJ}}(R_i) = \varepsilon \left[\frac{6}{n(R_i) - 6} \left(\frac{R_m}{R_i} \right)^{n(R_i)} - \frac{n(R_i)}{n(R_i) - 6} \left(\frac{R_m}{R_i} \right)^6 \right] \tag{17}$$

where R_i describes the distance between the He atom and the C or S atom, which depends on the intermolecular R and the intramolecular r separation distances and on the angle Θ (see Fig. 1). Moreover, ε and R_m represent the depth and the minimum location, respectively, of the pair interaction potential well. These potential parameters have been evaluated from the *effective* polarizability of each atom within the CS molecule in accordance with the general guidelines reported in ref.[76]. The effective atomic polarizability of interest (which is different from that of the isolated atom) is obtained by partitioning the CS molecular polarizability, given in Fig. 8, at each intramolecular distance r, while the polarizability of He is taken from[77]. The analytical profile of the CS molecular polarizability, reported in the lower panel of Fig. 8 as a solid line, is expressed in a similar way as previously obtained for the CO molecule (see Appendix A of Ref.[66]).
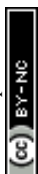
The term $n(R_i)$ is:

$$n(R_i) = \beta_i(r) + 4\left(\frac{R_i}{R_m}\right)^2 \qquad (18)$$

where $\beta_i(r)$, depending on the hardness of the interacting partners, a property that relates to their polarizability[78], is modulated by the CS stretching Δr. Accordingly, the following empirical formula has been adopted to provide reliable $\beta_i(r)$ values even for large CS deformations, associated with high vibrational levels close to the molecular dissociation:

$$\beta_i(r) = \beta_i^{eq} + \beta_i^1\left(-\Delta r + \frac{1}{2}\Delta r^2 + \frac{1}{2}\Delta r^3 - \frac{1}{4}\Delta r^4\right). \qquad (19)$$

CS is characterized by a very large equilibrium distance. Its outer electronic charge distribution is highly anisotropic, defining the strength of the repulsion at each orientation angle Θ, and it cannot be represented as a combination of two spheres contributions related to the size of the two atoms. Accordingly, the sum of the two $V_{ILJ}(R_i)$ components, characterizing previous formulations, has been corrected here with the addition of the term $V_{rep}(R,\Theta)$, which varies significantly with both the intermolecular distance and the molecular orientation:

$$V_{rep}(R,\Theta) = c_{rep}e^{-3R}\sin^6(\Theta). \qquad (20)$$

For the two interacting pairs, the adopted ε and R_m, evaluated at the equilibrium distance r_{eq}, and the other potential parameters are given in Table 1. Note that the zeroth order values of ε and R_m, predicted by the atomic polarizabilities of the interacting pairs, have been fine-tuned (R_m by 2-3% and ε by 10-15%) to achieve the best comparison with the *ab initio* points.

Table 1 Parameters for the analytical potential energy surface at $r = r_{eq}$.

Parameter	Value
r_{eq}^{CS} (Å)	1.5346
$\mu_{r_{eq}}^{CS}$ (ea_0)	0.7758
R_m^{S-He} (Å)	3.74
R_m^{C-He} (Å)	3.85
ε^{S-He} (meV)	2.00
ε^{C-He} (meV)	1.28
β_{S-He}^{eq}	8.0
β_{C-He}^{eq}	8.2
β_{S-He}^1	2.0
β_{C-He}^1	6.0
c_{rep} (meV)	70000

The new PES behaves correctly upon deformation of the CS bond thanks to the physically meaningful parameters of its formulation. This is clear from the trend of the analytical expressions for the CS polarizability and dipole moment as a function of r (Fig. 8). These values are in good agreement with the ab initio predictions.

References

1 I. V. Adamovich and W. R. Lempert, Plasma Physics and Controlled Fusion, 2014, 57, 014001.

Fig. 8 CS dipole moment (upper panel) and molecular polarizability (lower panel) as a function of the intramolecular distance. Solid lines correspond to the analytical expressions (see text).

2 R. Celiberto, I. Armenise, M. Cacciatore, M. Capitelli, F. Esposito, P. Gamallo, R. K. Janev, A. Laganà, V. Laporta, A. Laricchiuta, A. Lombardi, M. Rutigliano, R. Sayós, J. Tennyson and J. M. Wadehra, Plasma Sources Science and Technology, 2016, 25, 033004.

3 C. D. Pintassilgo and V. Guerra, The Journal of Physical Chemistry C, 2016, 120, 21184–21201.

4 A. V. Pavlov, Geomagnetism and Aeronomy, 2011, 51, 143–169.

5 V. Yankovsky and E. Vorobeva, Atmosphere, 2020, 11, 116.

6 M. Keidar, Plasma Sources Science and Technology, 2015, 24, 033001.

7 E. Roueff and F. Lique, Chemical Reviews, 2013, 113, 8906–8938.

8 J. Tennyson, S. N. Yurchenko, J. Zhang, C. A. Bowesman, R. P. Brady, J. Buldyreva, K. L. Chubb, R. R. Gamache, M. N. Gorman, E. R. Guest, C. Hill, K. Kefala, A. Lynas-Gray, T. M. Mellor, L. K. McKemmish, G. B. Mitev, I. I. Mizus, A. Owens, Z. Peng, A. N. Perri, M. Pezzella, O. L. Polyansky, Q. Qu, M. Semenov, O. Smola, A. Solokov, W. Somogyi, A. Upadhyay, S. O. Wright and N. F. Zobov, Journal of Quantitative Spectroscopy and Radiative Transfer, 2024, 326, 109083.

9 M. Capitelli, I. Armenise, E. Bisceglie, D. Bruno, R. Celiberto, G. Colonna, G. D'Ammando, O. De Pascale, F. Esposito, C. Gorse et al., Plasma Chemistry and Plasma Processing, 2012, 32, 427–450.

10 M. González-Martínez, W. Arbelo-González, J. Rubayo-Soneira, L. Bonnet and J.-C. Rayez, Chemical Physics Letters, 2008, 463, 65–71.

11 D. S. Lambrecht, G. N. I. Clark, T. Head-Gordon and M. Head-Gordon, The Journal of Physical Chemistry A, 2011, 115, 5928–5935.

12 G. D. Billing, Computer Physics Communications, 1984, 32, 45–62.

13 G. D. Billing, Computer Physics Reports, 1984, 1, 237–296.
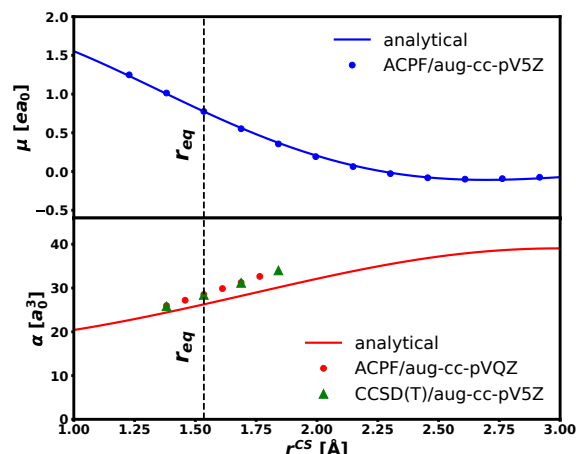
14 B. Mandal, D. Bostan, C. Joy and D. Babikov, Computer

Physics Communications, 2024, **294**, 108938.

15 Q. Hong, L. Storchi, Q. Sun, M. Bartolomei, F. Pirani and C. Coletti, Journal of Chemical Theory and Computation, 2023, **19**, 8557–8571.

16 M. Kirste, L. Scharfenberg, J. Kłos, F. Lique, M. H. Alexander, G. Meijer and S. Y. T. van de Meerakker, Physical Review A, 2010, **82**, 042717.

17 Y. Ajili, K. Hammami, N. E. Jaidane, M. Lanza, Y. N. Kalugina, F. Lique and M. Hochlaf, Physical Chemistry Chemical Physics, 2013, **15**, 10062–10070.

18 F. Daniel, M. Gérin, E. Roueff, J. Cernicharo, N. Marcelino, F. Lique, D. C. Lis, D. Teyssier, N. Biver and D. Bockelée-Morvan, Astronomy and Astrophysics, 2013, **560**, A3.

19 T. Stoecklin, O. Denis-Alpizar and P. Halvick, Monthly Notices of the Royal Astronomical Society, 2015, **449**, 3420–3425.

20 O. Denis-Alpizar and T. Stoecklin, Monthly Notices of the Royal Astronomical Society, 2015, **451**, 2986–2990.

21 O. Denis-Alpizar, T. Stoecklin, A. Dutrey and S. Guilloteau, Monthly Notices of the Royal Astronomical Society, 2020, **497**, 4276–4281.

22 Q. Hong, M. Bartolomei, C. Coletti, A. Lombardi, Q. Sun and F. Pirani, Molecules, 2021, **26**, 7152.

23 Q. Hong, Q. Sun, M. Bartolomei, F. Pirani and C. Coletti, Physical Chemistry Chemical Physics, 2020, **22**, 9375–9387.

24 Q. Hong, Q. Sun, F. Pirani, M. A. Valentín-Rodríguez, R. Hernández-Lamoneda, C. Coletti, M. I. Hernández and M. Bartolomei, The Journal of Chemical Physics, 2021, **154**, 064304.

25 Q. Hong, L. Storchi, C. Coletti, J. Li, Q. Sun and J. Li, The Journal of Chemical Physics, 2024, **160**, 084305.

26 Q. Hong, M. Bartolomei, F. Pirani, Q. Sun and C. Coletti, Journal of Chemical Physics, 2025, **162**, 114308.

27 A. Penzias, P. Solomon, R. Wilson and K. Jefferts, Astrophysical Journal, 1971, **168**, L53.

28 R. N. Martin and A. H. Barrett, Astrophysical Journal Letters, 1975, **202**, L83–L86.

29 C. Henkel and J. Bally, Astronomy and Astrophysics, 1985, **150**, L25–L27.

30 K. Drdla, G. R. Knapp and E. F. van Dishoeck, Astrophysical Journal, 1989, **345**, 815.

31 C. Sánchez Contreras, V. Bujarrabal and J. Alcolea, Astronomy and Astrophysics, 1997, **327**, 689–698.

32 M. Agúndez, J. P. Fonfría, J. Cernicharo, C. Kahane, F. Daniel and M. Guélin, Astronomy and Astrophysics, 2012, **543**, A48.

33 R. Le Gal, K. I. Öberg, R. A. Loomis, J. Pegues and J. B. Bergner, The Astrophysical Journal, 2019, **876**, 72.

34 S.-M. Tsai, E. K. Lee, D. Powell, P. Gao, X. Zhang, J. Moses, E. Hébrard, O. Venot, V. Parmentier, S. Jordan et al., Nature, 2023, **617**, 483–487.

35 F. Lique, A. Spielfiedel and J. Cernicharo, Astronomy and Astrophysics, 2006, **451**, 1125–1132.

36 F. Lique and A. Spielfiedel, Astronomy and Astrophysics, 2007, **462**, 1179–1185.

37 O. Denis-Alpizar, T. Stoecklin, P. Halvick, M.-L. Dubernet and S. Marinakis, The Journal of Chemical Physics, 2012, **137**, 234301.

38 O. Denis-Alpizar, T. Stoecklin, P. Halvick and M.-L. Dubernet, The Journal of Chemical Physics, 2013, **139**, 204304.

39 O. Denis-Alpizar, T. Stoecklin, S. Guilloteau and A. Dutrey, Monthly Notices of the Royal Astronomical Society, 2018, **478**, 1811–1817.

40 B. Yang, P. Zhang, C. Qu, P. C. Stancil, J. M. Bowman, N. Balakrishnan and R. C. Forrey, Physical Chemistry Chemical Physics, 2018, **20**, 28425–28434.

41 R. Goldflam, D. J. Kouri and S. Green, The Journal of Chemical Physics, 1977, **67**, 5661–5675.

42 R. Goldflam, S. Green and D. Kouri, The Journal of Chemical Physics, 1977, **67**, 4149–4161.

43 M. L. Dubernet, C. Boursier, O. Denis-Alpizar, Y. A. Ba, N. Moreau, C. M. Zwölf, M. A. Amor, D. Babikov, N. Balakrishnan, C. Balança, M. Ben Khalifa, A. Bergeat, C. T. Bop, L. Cabrera-González, C. Cárdenas, A. Chefai, P. J. Dagdigian, F. Dayou, S. Demes, B. Desrousseaux, F. Dumouchel, A. Faure, R. C. Forrey, J. Franz, R. M. García-Vázquez, F. Gianturco, A. Godard Palluet, L. González-Sánchez, G. C. Groenenboom, P. Halvick, K. Hammami, F. Khadri, Y. Kalugina, I. Kleiner, J. Kłos, F. Lique, J. Loreau, B. Mandal, B. Mant, S. Marinakis, D. Ndaw, P. Pirlot Jankowiak, T. Price, E. Quintas-Sánchez, R. Ramachandran, E. Sahnoun, C. Santander, P. C. Stancil, T. Stoecklin, J. Tennyson, F. Tonolo, R. Urzúa-Leiva, B. Yang, E. Yurtsever and M. Żółtowski, Astronomy and Astrophysics, 2024, **683**, A40.

44 F. Pirani, S. Brizi, L. Roncaratti, P. Casavecchia, D. Cappelletti and F. Vecchiocattivi, Physical Chemistry Chemical Physics, 2008, **10**, 5489–5503.

45 P. Ehrenfest, Zeitschrift für physik, 1927, **45**, 455–457.

46 R. Ram, P. Bernath and S. Davis, Journal of Molecular Spectroscopy, 1995, **173**, 146–157.

47 H. Uehara, K. Horiai and Y. Sakamoto, Journal of Molecular Spectroscopy, 2015, **313**, 19–39.

48 N. R. Crockett, E. A. Bergin, J. L. Neill, C. Favre, P. Schilke, D. C. Lis, T. A. Bell, G. Blake, J. Cernicharo, M. Emprechtinger, G. B. Esplugues, H. Gupta, M. Kleshcheva, S. Lord, N. Marcelino, B. A. McGuire, J. Pearson, T. G. Phillips, R. Plume, F. van der Tak, B. Tercero and S. Yu, The Astrophysical Journal, 2014, **787**, 112.

49 C. A. Bowesman, S. N. Yurchenko, A. Al-Refaie and J. Tennyson, TIRAMISU: Non-LTE radiative transfer for molecules in exoplanet atmospheres, 2025, https://arxiv.org/abs/2508.12873.

50 C. C. Marston and G. G. Balint-Kurti, Journal of Chemical Physics, 1989, **91**, 3571–3576.

51 R. J. Le Roy, Journal of Quantitative Spectroscopy and Radiative Transfer, 2017, **186**, 158–166.

52 M. Bogey, C. Demuynck and J. Destombes, Journal of Molecular Spectroscopy, 1982, **95**, 35–42.

53 G. Paulose, E. J. Barton, S. N. Yurchenko and J. Tennyson, Monthly Notices of the Royal Astronomical Society, 2015,

454, 1931–1939.

54 J. A. Coxon and P. G. Hajigeorgiou, Chemical Physics, 1992, **167**, 327–340.

55 T. Furtenbacher, A. G. Császár and J. Tennyson, Journal of Molecular Spectroscopy, 2007, **245**, 115–125.

56 R. J. Le Roy, Journal of Quantitative Spectroscopy and Radiative Transfer, 2017, **186**, 167–178.

57 R. A. Kendall, T. H. Dunning and R. J. Harrison, The Journal of Chemical Physics, 1992, **96**, 6796–6806.

58 H.-J. Werner, B. Follmeg and M. H. Alexander, The Journal of Chemical Physics, 1988, **89**, 3139–3151.

59 J. Yang, Q. Hong, M. Bartolomei, C. Coletti, F. Pirani, Q. Sun and J. Li, Physical Review A, 2025, **111**, 032804.

60 S. Boys and F. Bernardi, Molecular Physics, 1970, **19**, 553–566.

61 A. Halkier, T. Helgaker, P. Jorgensen, W. Klopper, H. Koch, J. Olsen and A. K. Wilson, Chemical Physics Letters, 1998, **286**, 243–252.

62 A. Halkier, T. Helgaker, P. Jorgensen, W. Klopper, J. Olsen and A. K. Wilson, Chemical Physics Letters, 1999, **302**, 437–446.

63 M.Bartolomei, E. Carmona-Novillo, M. I. Hernández, J. Campos-Martínez and R. Hernández-Lamoneda, Journal of Computational Chemistry, 2011, **32**, 279–290.

64 M.Bartolomei, F. Pirani, A. Laganà and A. Lombardi, Journal of Computational Chemistry, 2012, **33**, 1806–1819.

65 A. Lombardi, F. Pirani, A. Laganà and M.Bartolomei, Journal of Computational Chemistry, 2016, **37**, 1463–1475.

66 A. Lombardi, F. Pirani, M.Bartolomei, C. Coletti and A. Laganà, Frontiers in Chemistry, 2019, **7**, 309.

67 H.-J. Werner, P. J. Knowles, R. Lindh, F. R. Manby, M. Schütz, P. Celani, T. Korona, G. Rauhut, R. D. Amos, A. Bernhardsson, A. Berning, D. L. Cooper, M. J. O. Deegan, A. J. Dobbyn, F. Eckert, C. Hampel, G. Hetzer, A. W. Lloyd, S. J. McNicholas, W. Meyer, M. E. Mura, A. Nicklass, P. Palmieri, R. Pitzer, U. Schumann, H. Stoll, A. J. Stone, R. Tarroni and T. Thorsteinsson, MOLPRO, Version 2012.1, a Package of Ab Initio Programs, 2012, see http://www.molpro.net.

68 J. Arnold, J. C. San Vicente Veliz, D. Koner, N. Singh, R. J. Bemish and M. Meuwly, The Journal of Chemical Physics, 2022, **156**, 034301.

69 Q. Hong, L. Storchi, M. Bartolomei, F. Pirani, Q. Sun and C. Coletti, European Physical Journal D, 2023, **77**, 128.

70 J. Yang, J. Li, J. Li and J. Li, The Journal of Physical Chemistry A, 2024.

71 D. Bossion, G. Nyman and Y. Scribano, Artificial Intelligence Chemistry, 2024, **2**, 100052.

72 L. Storchi, CurveFittingML, 2022, https://github.com/lstorchi/CurveFittingML.

73 D. R. Flower, Monthly Notices of the Royal Astronomical Society, 2012, **425**, 1350–1356.

74 M. Pezzella, F. Pirani, M. Bartolomei, Q. Hong, F. Lique, L. Storchi and C. Coletti, DATA related to: Vibrational relaxation rate coefficients in CS-He collisions up to the dissociation limit: mixed quantum-classical calculations and neural network predictions, 2025, https://doi.org/10.5281/zenodo.17554162.

75 G. C. Maitland, M. Rigby, E. B. Smith and W. A. Wakeham, Intermolecular Forces: Their Origin and Determination, Clarendon Press, Oxford, 1987.

76 R. Cambi, D. Cappelletti, G. Liuti and F. Pirani, The Journal of chemical physics, 1991, **95**, 1852–1861.

77 T. N. Olney, N. Cann, G. Cooper and C. Brion, Chemical Physics, 1997, **223**, 59–98.

78 M. Capitelli, D. Cappelletti, G. Colonna, C. Gorse, A. Laricchiuta, G. Liuti, S. Longo and F. Pirani, Chemical Physics, 2007, **338**, 62–68.

Data Availability

The data supporting this article, including the routine for the analytical PES, are available as part of the Supplementary Information or can be found in the following repositories:

 Neural Network codes: CurveFittingML, 2022, https://github.com/lstorchi/CurveFittingML.

Trained Neural Network models and rate coefficient datasets: M. Pezzella, F. Pirani, M. Bartolomei, Q. Hong, F. Lique, L. Storchi and C. Coletti, DATA related to: Vibrational relaxation rate coefficients in CS-He collisions up to the dissociation limit: mixed quantum-classical calculations and neural network predictions, 2025, https://doi.org/10.5281/zenodo.17554162.

Physical Chemistry Chemical Physics Accepted Manuscript